Proceedings of the 12th International and 52nd National Conference on Fluid Mechanics and Fluid Power (FMFP)
December 19-21, 2025, Nirma University, Gujarat, India

FMFP2025–BFM–353

CFD Analysis of Full-Cycle Nasal Airflow in a Standardized Human Geometry Under Realistic Breathing Patterns

Makesh Singh[1], Shashwat Bhattacharya[1], and Gaurav Bhutani[1,*]

[1]School of Mechanical and Materials Engineering, Indian Institute of Technology Mandi, Himachal Pradesh 175075, India
* Corresponding Author, email: gaurav@iitmandi.ac.in

ABSTRACT

Transient, full-cycle CFD simulations of nasal airflow were performed in a standardized human nasal geometry reconstructed from averaged CT cross-sections. The incompressible, Newtonian flow was solved using the finite-volume method. A sinusoidal pressure waveform was imposed at the nasopharynx via a user-defined function while the nostril boundary was held at ambient pressure. A multi-mesh grid-independence study identified mesh convergence and strong-scaling tests on the PARAM Himalaya cluster indicated optimal performance at 35 cores. Simulations for normal breathing, exercise, and sniffing produced mass-conservative solutions with Reynolds numbers at representative sections ranging from 793 to 1,099, supporting a laminar modeling approach. Peak inlet velocities rose with respiratory effort: 5.81 m/s (normal), 12.08 m/s (exercise), and 19.30 m/s (sniffing), accompanied by larger pressure gradients and localized inhalation jets. These results quantify full-cycle nasal dynamics in a population-representative geometry and provide benchmark data for inhalation physiology studies, particle transport analyses, and numerical best practices in nasal CFD.

Keywords: Nasal airflow; Computational fluid dynamics; Standardized nasal geometry; Breathing patterns

I. INTRODUCTION

The human nasal cavity performs vital functions: it warms, humidifies and filters inhaled air while directing flow to the lower airways. Its internal geometry is narrow, curved and asymmetric, so even ordinary breathing produces complex local flow patterns. Flow regime changes with breathing intensity. During normal breathing the flow is mostly steady or weakly disturbed, during exercise it becomes unsteady and may transition to turbulence, and during a short rapid inhalation (sniff) strong transient jets and vortices develop. Because of this complexity, accurate prediction of velocity, pressure and mass flow in the nasal passages is essential for diagnosis, surgical planning and inhaled drug delivery. Computational fluid dynamics (CFD) has become a widely-used tool since it provides detailed spatial and temporal information that experiments cannot easily capture.

A number of studies have examined nasal airflow across a range of breathing conditions. Resting, exercising, and sniffing flows have been compared in CT-based patient geometries, with careful mesh verification and validation [1]. High-resolution transient simulations have characterized short inhalations, emphasizing the need for temporal convergence [2]. Scale-resolving approaches have been used to analyze pressure distributions at various inhalation rates [3, 4], while large-eddy simulations have captured intricate vortical structures during sniffing and high-flow regimes [5].

Despite these advances, most CFD studies rely on patient-specific geometries, which limits the generalizability of their findings. Moreover, they primarily focus on inspiratory flow, overlooking the complex dynamics of the full breathing cycle. The present work addresses these gaps by employing a standardized nasal cavity geometry generated through statistical averaging of multiple healthy participants [6], enabling the study of normative flow conditions. We analyze complete inhalation–exhalation cycles under normal breathing, exercise, and sniffing conditions to provide physiological context for flow-regime classification across different respiratory intensities.

This paper is organized as follows. Section II describes the mathematical formulation, numerical methods, and simulation setup, including details of the geometry reconstruction, meshing strategy, and grid-independence analysis. Section III presents and discusses the transient CFD results for normal breathing, exercise, and sniffing conditions, focusing on mass flow characteristics, flow regimes, and detailed pressure and velocity fields throughout the nasal cavity. Section IV concludes the study by summarizing the key findings, highlighting methodological insights, and outlining directions for future work.

II. METHODOLOGY

A. Governing Equations and Discretization

The airflow in the nasal cavity was modeled as a single-phase, incompressible, laminar flow with a Newtonian constitutive model. The governing equations consist of the continuity and momentum equations for incompressible flow. The continuity equation ensures mass conservation and is given by

$$\nabla \cdot \mathbf{u} = 0, \tag{1}$$

where $\mathbf{u}$ is the velocity vector. The conservation of linear momentum is expressed through the unsteady, incompressible Navier–Stokes equations as

$$\rho \left(\frac{\partial \mathbf{u}}{\partial t} + \mathbf{u} \cdot \nabla \mathbf{u} \right) = -\nabla p + \mu \nabla^2 \mathbf{u}, \tag{2}$$

where ρ is the fluid density, p is the static pressure, and μ is the dynamic viscosity.

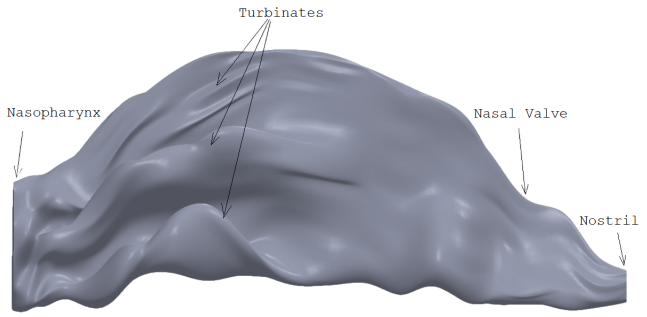

Figure 1: **Reconstructed right-side nasal cavity geometry based on averaged coronal CT data, used as the standardized domain for CFD simulations.**

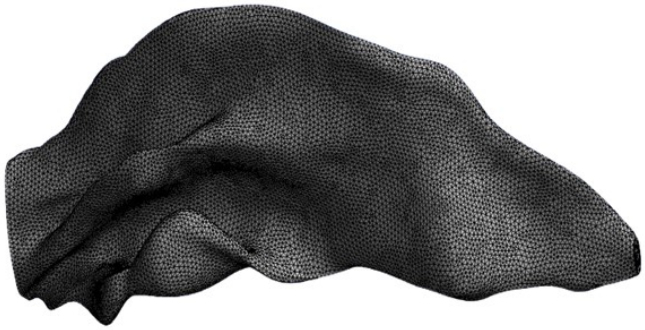

Figure 2: **Tetrahedral mesh of the standardized nasal cavity model used for CFD simulations.**

The governing equations were discretized using the finite-volume method in ANSYS® Fluent 18.1. Pressure–velocity coupling was achieved using the SIMPLE algorithm with Rhie–Chow momentum-based flux interpolation. A least-squares cell-based scheme was employed for gradient evaluation, while pressure was discretized using a second-order scheme and momentum convection terms using a second-order upwind scheme. Temporal discretization was performed using a first-order implicit formulation. The model geometry, meshing, and numerical setup are described in the subsequent subsections.

B. Geometry and Mesh

The nasal cavity geometry was reconstructed following the methodology of Liu et al. (2022) [7], who developed a standardized three-dimensional median nasal model by collecting, aligning, and combining coronal Computed Tomography (CT) slices from multiple subjects to generate representative cross-sections and a continuous surface. The averaged coronal profiles and measurements from their study were used as templates to build the right-side nasal passage for CFD analysis in the present work. Key anatomical features such as the nostril inlet, nasal valve, and turbinate contours were retained to ensure physiological realism.

The selected cross-sectional data were digitized and used to create a smooth, watertight three-dimensional model in SolidWorks®. The geometry was constrained to match the reference medians in overall length and local cross-sectional area, resulting in a standardized and representative physical domain. The final right-side nasal cavity model, representing a general median-based nasal airway, is shown in Figure 1.

The completed geometry was exported in a CAD exchange format and imported into ANSYS® Fluent, where it served as the computational domain for meshing and flow simulations. Key anatomical landmarks relevant to airflow—such as the nostrils, nasal valve, turbinates, and nasopharynx—were preserved, while small-scale features with negligible influence on the bulk flow were omitted. This approach ensured an effective balance between anatomical fidelity and numerical tractability, yielding a standardized model suitable for comparative CFD studies and reproducible simulation of inspiratory airflow. The resulting nasal cavity model was approximately 60 mm long and 35 mm wide, representative of the typical adult nasal passage dimensions.

Meshing was carried out in the ANSYS® Meshing utility using tetrahedral elements to discretize the computational domain, as shown in Figure 2.

C. Simulation Setup

A pressure-outlet boundary condition was applied at the nasopharynx, where a sinusoidal pressure variation was prescribed as a function of time using a User-Defined Function (UDF) (Fig. 3). The imposed waveform had a respiratory period of $T = 4$ s with an inspiratory-to-expiratory ratio of $1 : 1$. A pressure-inlet boundary condition with $p = 0$ was set at the nostrils to represent ambient atmospheric pressure. The nasal cavity walls were assumed to be rigid and stationary, with a no-slip condition applied at all solid boundaries. A fixed time-step size of $\Delta t = 1 \times 10^{-4}$ s was used for all simulations. For this choice of Δt, the Courant–Friedrichs–Lewy (CFL) number remained well below unity across all mesh resolutions, ensuring numerical stability and temporal accuracy. The fluid was modeled as air with a density of $\rho = 1.2041$ kg/m^3 and a dynamic viscosity of $\mu = 1.81 \times 10^{-5}$ Pa $\cdot$ s.

All simulations were executed on the PARAM Himalaya supercomputing cluster, which is powered by Intel® Xeon® Platinum 8268 processors. A strong scaling test was performed to assess the parallel performance of the CFD solver on this architecture. The scaling analysis was carried out using a simulation time of 1 s, corresponding to half of the inhalation phase, in order to keep the computational cost manageable while retaining representative flow physics. Figure 4 shows the variation of total simulation time with the number of compute cores. A significant reduction in runtime was observed when increasing the core count from 25 to 30. The minimum simulation time was achieved at 35 cores, beyond which the runtime increased, indicating diminishing parallel efficiency and the onset of communication overheads at higher core counts. This trend reflects typical strong scaling behavior, with 35 cores representing the optimal balance between computational cost and parallel performance for the present problem size. The M3 mesh, which is described in the next subsection, was used for the scaling analysis. Based

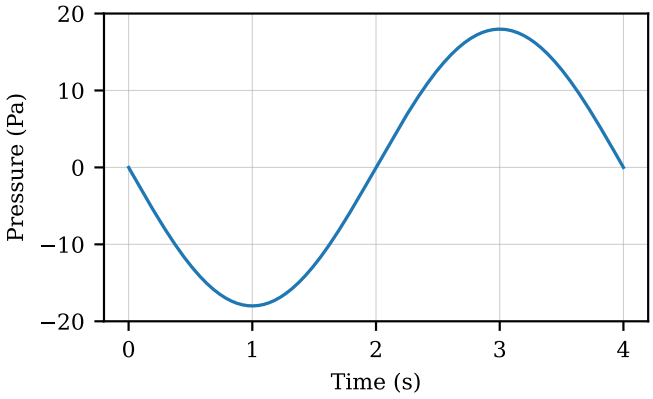

Figure 3: **Time-varying sinusoidal pressure waveform imposed at the nasopharynx through a user-defined function as a boundary condition for a complete breathing cycle.**

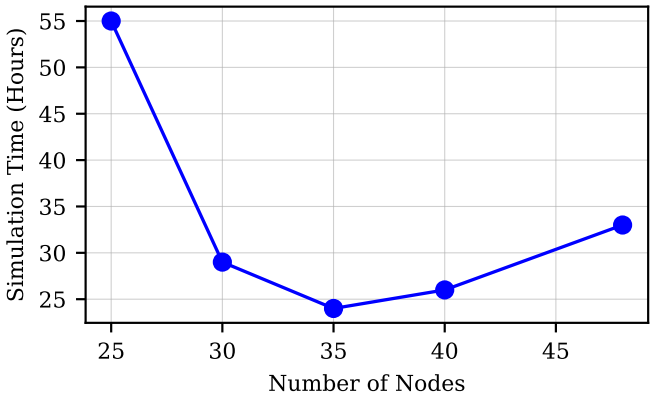

Figure 4: **Strong scaling test on the PARAM Himalaya supercomputing cluster showing the variation of total simulation time with the number of compute cores.**

on these results, all subsequent simulations in this study were performed using 35 compute cores.

D. Grid-Independence Study

A grid-independence study was carried out to ensure that the numerical results were insensitive to mesh resolution. Four unstructured tetrahedral meshes (M1–M4) with increasing element counts were generated for this purpose. The mesh characteristics, including the number of nodes (N_n), number of elements (N_e), and nominal grid size (Δ) are summarized in Table 1.

The area-average-velocity timeseries at the nasopharynx for all four meshes are compared in Fig. 5. A significant change in the solution was observed when refining from M1 to M2, whereas further refinement from M2 to M3 and M4 led to negligible differences. The velocity curves for M3 and M4 are practically identical, indicating mesh convergence. Based on these results, the M3 mesh was selected for all subsequent simulations as it offers a good compromise between accuracy and computational cost.

Table 1: **Mesh resolution parameters for the grid-independence study. All meshes consist of tetrahedral elements.**

Mesh	$\mathbf{N_e}$ $(\times\mathbf{10^6})$	$\mathbf{N_n}$ $(\times\mathbf{10^6})$	$\mathbf{\Delta}$ $\mathbf{(mm)}$
M1	0.05	0.025	1.0
M2	0.15	0.100	0.5
M3	0.25	0.136	0.4
M4	0.36	0.170	0.7

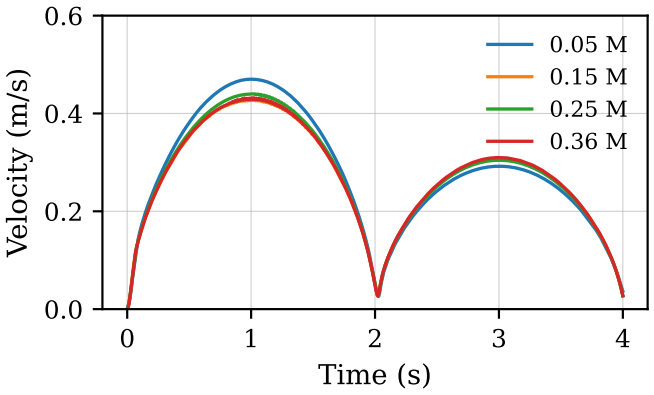

Figure 5: **Comparison of the average-velocity timeseries at nasopharynx for different mesh resolutions (M1–M4), demonstrating mesh convergence. Figure legend presents the number of mesh nodes for the four meshes.**

III. RESULTS AND DISCUSSION

The results of the transient CFD simulations are presented and discussed in this section. The analysis focuses on three key aspects: (i) characterization of the overall flow behavior through mass flow rate histories and Reynolds number evaluation, (ii) detailed examination of the pressure and velocity fields within the nasal cavity during normal breathing, and (iii) comparison of flow characteristics across different respiratory maneuvers, namely normal breathing, exercising, and strong sniffing. Together, these analyses provide a comprehensive picture of nasal airflow dynamics under realistic, full-cycle breathing conditions.

A. Mass Flow Rate and Flow Regime

The transient simulations capture the cyclic variation of mass flow rates at the nostrils (inlet) and nasopharynx (outlet) during a complete breathing cycle. As shown in Figure 6, the mass flow rates at the two boundaries oscillate sinusoidally with equal magnitude, confirming overall mass conservation. This behavior reflects the physiological breathing cycle, with airflow entering through the nostrils during inhalation and exiting through the nasopharynx during exhalation, thereby validating the temporal accuracy and stability of the numerical setup.

To characterize the flow regime within the nasal cavity, Reynolds numbers were evaluated at three representative cross-sections (Planes 1–1', 2–2', and 3–3'), as shown in

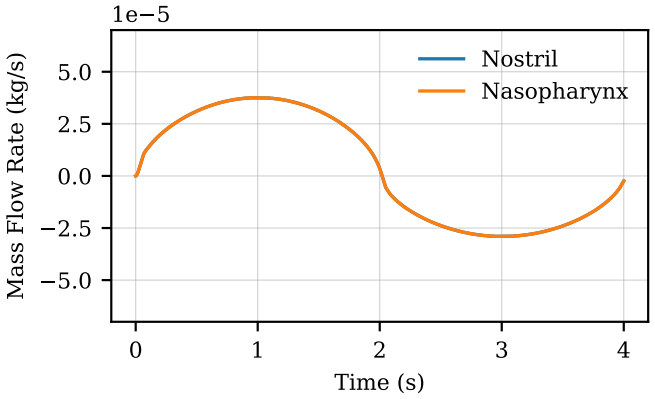

Figure 6: **Time variation of mass flow rate at the nostrils and nasopharynx during a complete breathing cycle. Both plots overlap demonstrating mass conservation.**

Figure 7. The Reynolds number was computed using

$$Re = \frac{U_{\text{avg}} D_h}{\nu},$$

where U_{avg} is the average velocity, D_h is the hydraulic diameter of the section, and ν is the kinematic viscosity of air. The corresponding geometric and flow parameters, along with the calculated Reynolds numbers, are summarized in Table 2.

Table 2: **Reynolds number calculation at three cross-sections.**

Plane	D_h (m)	U_{avg} (m/s)	Re
1–1’	0.010	1.604	1099
2–2’	0.022	0.541	793
3–3’	0.035	0.437	1005

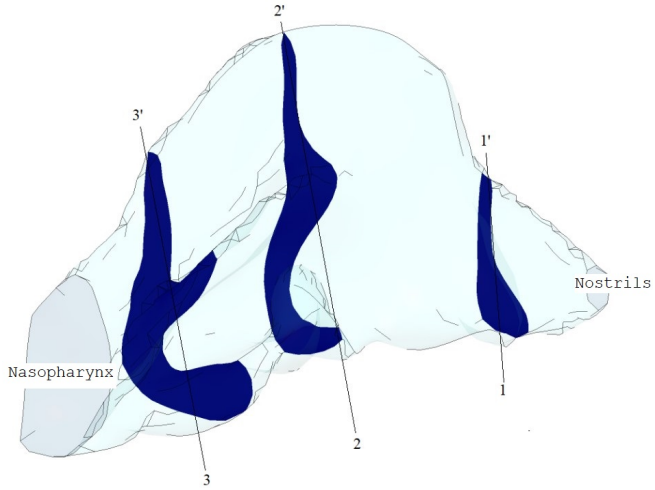

Figure 7: **Locations of the three cross-sectional planes used for Reynolds number calculation.**

For all three planes, the Reynolds number remained well below the critical value of 2000, indicating laminar flow throughout the nasal cavity. This justifies the use of the laminar flow model in the present CFD simulations.

B. Flow Field Analysis

CFD analysis of the nasal cavity revealed distinct pressure and velocity characteristics for the two phases of normal breathing, as shown in Figure 8. Inhalation was characterized by a high-velocity jet of air, reaching peak speeds of up to 4.84 m/s (see scale on bottom left), which was driven by a strong negative pressure gradient (down to -40 Pa as shown on the top-left color bar) relative to the surrounding environment. This suction effect efficiently draws air inward.

Conversely, exhalation was driven by a positive pressure gradient (up to 25 Pa on the top-right color bar), which pushed the air outward. The resulting airflow during exhalation was generally slower and more distributed, with a lower peak velocity compared to the active phase of inhalation.

C. Analysis of Breathing Flow Patterns

Figure 9 shows the variation of nasopharynx pressure over time for three breathing modes. Normal breathing [8] produces low-amplitude, smooth sinusoidal fluctuations. Exercising [9] results in larger and faster oscillations, while sniffing [10, 11, 12] generates the highest amplitude with sharp transient peaks. Among the different categories of sniffing (normal, medium, and strong), the present study focuses on strong sniffing, which exhibits the most intense flow features.

Analyzing normal breathing, exercising, and sniffing captures the full physiological range of nasal airflow. Normal breathing provides baseline ventilation characteristics relevant for diagnostic metrics. Exercising increases flow rates, resistance, and heat and moisture exchange, which are important for mask design, rehabilitation, and performance studies. Sniffing produces short, high-acceleration peaks that dominate olfaction and rapid particle deposition, informing clinical assessments, drug delivery, device design, and inhalation therapies.

The analysis of maximum airflow velocity in this work across these three respiratory maneuvers revealed a clear escalation in peak velocity with increasing breathing intensity, as shown in Figure 10. The maximum velocity was consistently observed at the nostrils for all conditions. During normal breathing, the peak nostril velocity reached 5.81 m/s, with a corresponding nasopharynx velocity of 0.43 m/s. For exercising, the peak nostril velocity increased by approximately 108%, reaching 12.08 m/s. The most intense maneuver, sniffing, produced the highest overall velocities, with a maximum nostril velocity of 19.30 m/s and an nasopharynx velocity of 2.03 m/s, confirming that sniffing generates the most rapid and intense nasal airflow.

IV. CONCLUSIONS

This study presented high-fidelity, full-cycle CFD simulations of airflow through a standardized human nasal cavity under three representative breathing conditions—normal breathing, exercising, and strong sniffing. The use of a statistically averaged nasal geometry enabled physiologically

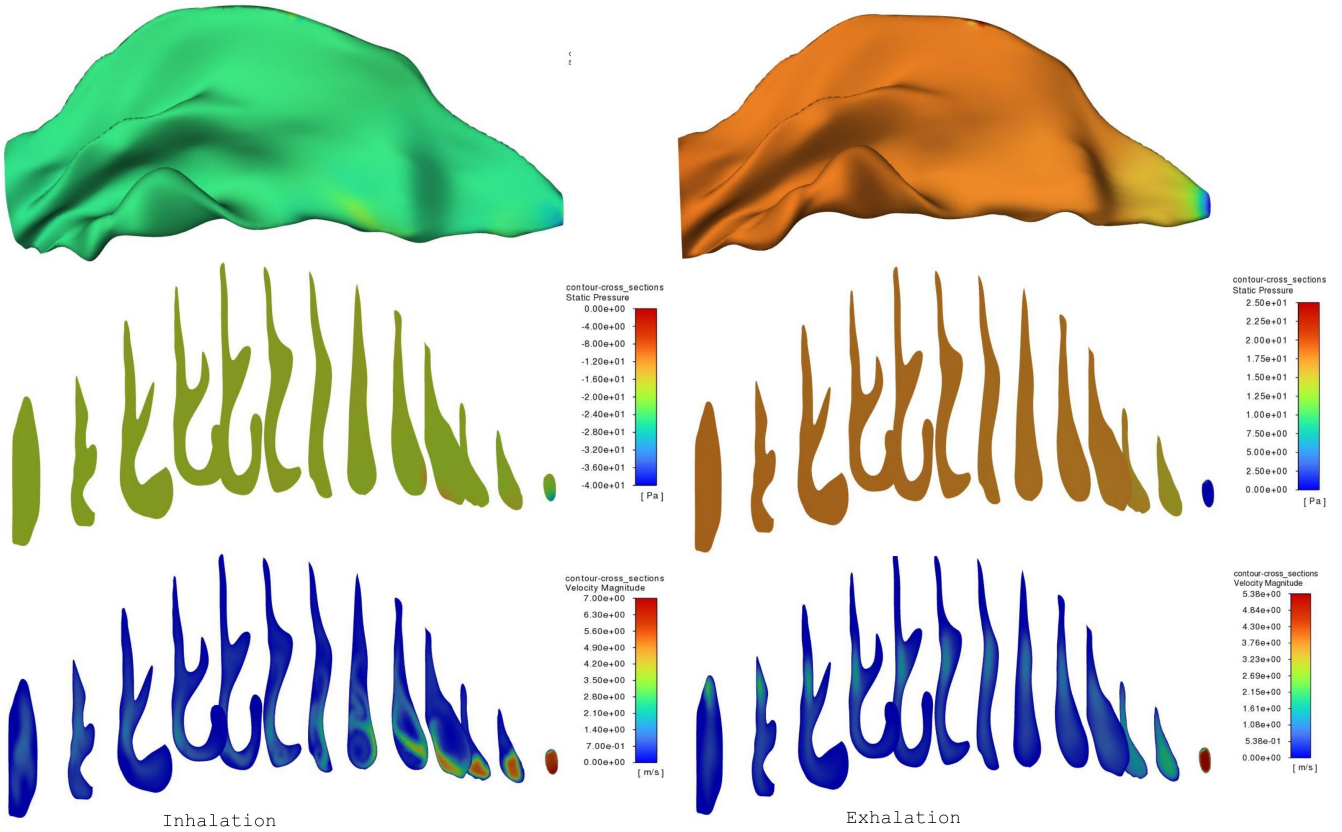

Figure 8: **Pressure (top) and velocity (bottom) contours during inhalation (left) and exhalation (right) for normal breathing, illustrating the distinct flow characteristics across coronal planes of the nasal cavity.**

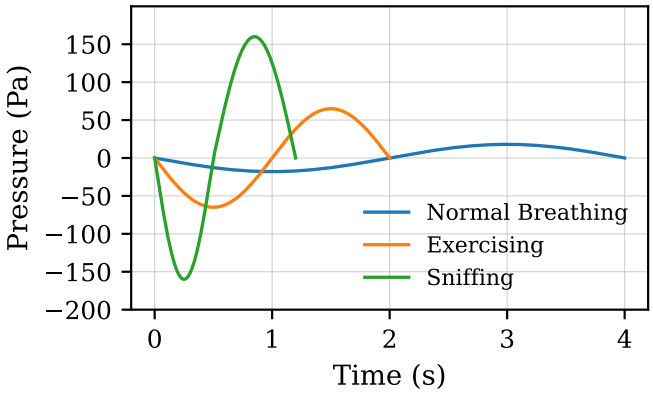

Figure 9: **Time variation of nasopharynx pressure for three different breathing conditions.**

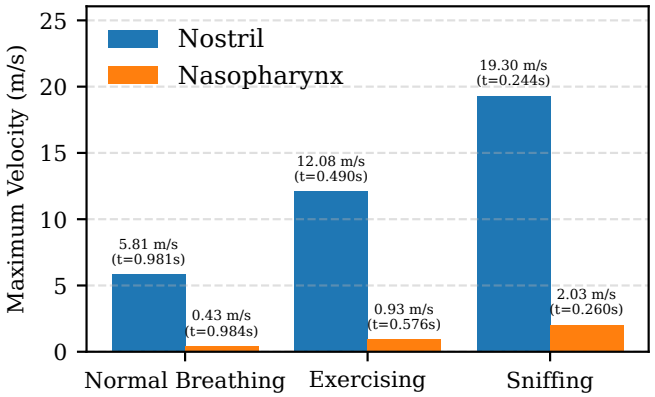

Figure 10: **Maximum airflow velocity at the nostrils and nasopharynx for different breathing conditions.**

representative and generalizable flow fields. Peak velocities increased from $5.8\ \mathrm{m/s}$ (normal) to $12.1\ \mathrm{m/s}$ (exercise) and $19.3\ \mathrm{m/s}$ (sniffing), accompanied by larger pressure gradients and localized jets. Despite these variations, Reynolds numbers across key sections remained well below 2000, confirming that laminar modeling is sufficient for all three breathing modes. Rigorous grid-independence and strong-scaling analyses ensured numerical accuracy and efficiency, providing practical guidelines for future nasal airflow simulations.

Beyond generating benchmark velocity and pressure distributions, the results establish a reproducible baseline for comparing numerical methods, breathing patterns, and inter-study variations, which is often lacking in patient-specific

studies. These findings support applications in clinical assessment, surgical planning, and inhaled drug delivery. Although the laminar model was found to be adequate based on Reynolds number estimates, future work may examine transitional or turbulence-resolving simulations—particularly for high-intensity sniffing where local flow acceleration and vortex formation could induce turbulent phenomena.

ACKNOWLEDGEMENTS

MS thanks the Ministry of Education, Government of India, for scholarship support during his PhD. The authors acknowledge the National Supercomputing Mission for computing resources on 'PARAM Himalaya' at IIT Mandi, supported by C-DAC, MeiTY, and DST, Government of India.

NOMENCLATURE

ρ	Density of air	$[\mathrm{kg/m^3}]$
v	Average velocity of air	$[\mathrm{m/s}]$
D_h	Hydraulic diameter of the cross-section	[m]
μ	Dynamic viscosity of air	$[\mathrm{kg/(m \cdot s)}]$
ν	Kinematic viscosity of air (μ/ρ)	$[\mathrm{m^2/s}]$

REFERENCES

[1] Chengyu Li, Jianbo Jiang, Haibo Dong, and Kai Zhao. Computational modeling and validation of human nasal airflow under various breathing conditions. *Journal of Biomechanics*, 64:59–68, 2017.

[2] Alister J Bates, Andreas Schuh, Gabriel Amine-Eddine, Keith McConnell, Wolfgang Loew, Robert J Fleck, Jason C Woods, Charles L Dumoulin, and Raouf S Amin. Assessing the relationship between movement and airflow in the upper airway using computational fluid dynamics with motion determined from magnetic resonance imaging. *Clinical Biomechanics*, 66:88–96, 2019.

[3] James Van Strien, Kendra Shrestha, Sargon Gabriel, Petros Lappas, David F Fletcher, Narinder Singh, and Kiao Inthavong. Pressure distribution and flow dynamics in a nasal airway using a scale resolving simulation. *Physics of Fluids*, 33(1), 2021.

[4] Syeda Reham Shahed, Jingliang Dong, Jiyuan Tu, and Lin Tian. Unsteady analysis of the airflow in human nasal airway – a computational study. *Computers in Biology and Medicine*, 191:110136, 2025.

[5] Paweł Niegodajew. Flow patterns and vortex formation mechanisms inside a human nasal cavity. *Physics of Fluids*, 37(2), 2025.

[6] Yuan Liu, Matthew R Johnson, Edgar A Matida, Safeema Kherani, and Joe Marsan. Creation of a standardized geometry of the human nasal cavity. *Journal of Applied Physiology*, 106(3):784–795, 2009.

[7] Yi Liu and Wan Lin Sun. Numerical analysis of nasal flow characteristics with microparticles. *Journal of Healthcare Engineering*, 2022(1):8706978, 2022.

[8] C. Li, T. Yu, D. Zhai, S. Liu, J. Liu, Y. Zhao, and Y. Zheng. Unsteady computational fluid dynamics simulation of a full breathing cycle in the human nasal cavity. *Journal of Biomechanics*, 71:201–210, 2018.

[9] Masaaki Suzuki and Tadashi Tanuma. The effect of nasal and oral breathing on airway collapsibility in patients with obstructive sleep apnea: Computational fluid dynamics analyses. *PLOS ONE*, 15(4):e0231262, 2020.

[10] Z. P. Xie, S. M. Xie, X. Zhang, et al. Computational fluid dynamics simulation of nasal airflow during sniffing in a healthy human nasal cavity. *Journal of Biomechanics*, 50(6):1234–1243, 2017.

[11] J. B. M. Kimbell, D. L. Sanderson, M. C. Rosso, et al. Nasal airflow patterns during sniffing: A study of normal subjects using computational fluid dynamics. *Laryngoscope*, 124(2):430–437, 2014.

[12] A. J. S. Lee, B. S. H. Chen, and F. H. M. Wong. Pressure drop and airflow in the nasal cavity during sniffing in normal subjects. *American Journal of Rhinology and Allergy*, 30(1):12–18, 2016.